THE JOURNAL OF PHYSICAL CHEMISTRY C

Article

pubs.acs.org/JPCC

Engineered Electronic States of Transition Metal Doped TiO_2 Nanocrystals for Low Overpotential Oxygen Evolution Reaction

Nitish Roy,[†] Youngku Sohn,[‡] Kam Tong Leung,[§] and Debabrata Pradhan*[,†]

[†]Materials Science Centre, Indian Institute of Technology, Kharagpur 721 302, W.B., India

[‡]Department of Chemistry, Yeungnam University, Gyeongsan, Gyeongbuk 712-749, Korea

[§]Department of Chemistry, University of Waterloo, Waterloo N2L 3G1, Ontario Canada

Supporting Information

ABSTRACT: Electrochemical oxygen evolution reaction (OER) involves high overpotential at the oxygen evolving electrode and thereby suffers significant energy loss in the proton exchange membrane water electrolyzer. To reduce the OER overpotential, precious ruthenium and iridium oxides are most commonly used as anode electrocatalyst. Here we report marked reduction in overpotential for the OER using transition metal (TM) doped TiO_2 nanocrystals (NCs). This reduction in overpotential is attributed to d-orbitals splitting of the doped TMs in the TM-doped TiO_2 NCs and their interactions with the oxyradicals (intermediates of OER) facilitating the OER. The d-orbital spitting of TMs in TM-doped TiO_2 NCs is evident from the change in original pearl white color of undoped TiO_2 NCs and UV−vis absorption spectra.

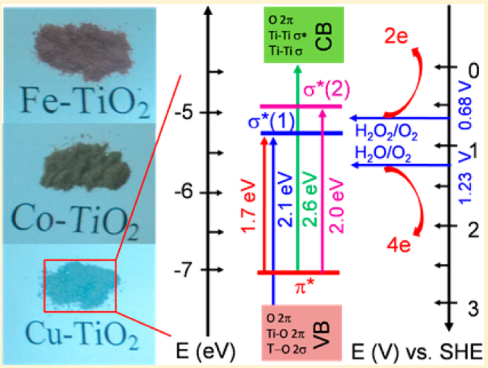

1. INTRODUCTION

TiO_2 is a prototype oxide material that has extensive applications in the field of photocatalytic degradation of organic contaminants, water splitting, pigments, self-cleaning, and dye sensitized solar cells.[1−5] Although TiO_2 is widely considered as a stable and potential catalyst for photochemical water-splitting reaction, it is poorly active for electrochemical oxygen evolution reaction (OER) and thus scarcely studied. Nonetheless, TiO_2 is a self-doped n-type material that has oxygen vacancy within its crystal. Such oxygen vacancy affects the physicochemical properties of TiO_2. In particular, oxygen vacancy reduces the band gap and hence increases the light absorption property.[6,7] In addition, surface oxygen vacancy serves as an electron donor center, an active site for heterogeneous catalysis, and enhances the electrical property, which thereby has strong influences on the photocatalytic and photoelectrochemical properties of TiO_2.[8] One of the simple ways to tune the oxygen vacancy is doping the metals or transition metals (TMs) within the crystal without changing the TiO_2 crystal structure and hence keeping the characteristics feature of TiO_2 intact while enhancing the aforesaid properties. For example, Nb-doped TiO_2 has recently been reported as a cathode catalyst for the oxygen reduction reaction of polymer electrolyte membrane (PEM) fuel cells.[9] Chevallier et al. demonstrated high stability with Nb-doped TiO_2 based catalyst support materials for the oxygen reduction reaction in a PEM fuel cell.[10] However, there are fewer studies on TiO_2 as electrocatalyst for OER.

One of the major challenges for a PEM water electrolyzer is to find an inexpensive electrocatalyst to replace commonly used precious metal oxides such as Ir_2O_3 and RuO_2 in the anode to reduce the overpotential of OER.[11−14] Thus, in recent years, attention has been focused on the preparation of inexpensive and non-noble metal oxide catalysts that could reduce the OER overpotential and improve the electrocatalytic activity.[15] This includes perovskites,[16] metal oxides,[17] and metal hydroxides/oxyhydroxides.[18,19] In particular, recently Hu et al. reported improved OER activity of IrO_2/Nb-TiO_2 catalyst as compared to unsupported IrO_2 catalyst.[11] This suggests the potential for TiO_2 as an electrocatalyst in addition to its advantageous properties of high thermal and chemical stability, lost cost, and commercial availability. Recently, Cai et al. reported enhanced OER with Co-doped TiO_2 nanowires synthesized by the sol-flame process.[20] A few other recent reports also confirm the reduction of OER overpotential with TM-doped TiO_2.[21,22] However, the exact rationality behind such improved performance remains unclear. Here we report reduced overpotential of OER using TM-doped TiO_2 nanocrystals (NCs) synthesized by a facile low-temperature hydrothermal technique. This reduced overpotential is attributed to d-orbital splitting of TMs in TiO_2 NCs producing midgap energy states as confirmed from the UV−vis absorption spectroscopy. The d-orbital splitting of three TMs (Fe, Co, and Cu) and their role in OER overpotential is discussed in the present report.

Received: August 21, 2014
Revised: December 2, 2014
Published: December 3, 2014

   dx.doi.org/10.1021/jp508445t | J. Phys. Chem. C 2014, 118, 29499−29506

2. EXPERIMENTAL DETAILS

2.1. Materials. All the chemicals were analytical grade and were used as received without further purification. Titanium tetraisopropoxide (TTIP) [99.999%], $Cu(NO_3)_2{\cdot}3H_2O$, $Fe(SO_4){\cdot}7H_2O$, $Co(NO_3)_2{\cdot}6H_2O$, tetrabutyl ammonium hydroxide (TBAH) [$(C_4H_9)_4NOH$ in 0.1 N aqueous], and diethanolamine (DEA) were purchased from Merck.

2.2. Synthesis of TM-Doped TiO_2 NCs. In a typical synthesis, 3 mmol of TTIP was added to a mixture of TBAH (40 mmol) and DEA (160 mmol), and the solution was stirred for 5 min at room temperature. Then the viscous solution was transferred to a Teflon-lined stainless steel autoclave and heated at 225 °C for 24 h. After the heat treatment, the autoclave was allowed to cool to room temperature naturally and the product was collected by centrifuge and washed with water and ethanol several times. The final product was dried in air at 60 °C for 24 h. The overall yield of the product was 90−95%. TM-doped TiO_2 NCs was synthesized by adding the corresponding salt of TM (2 mol %) to the solution of TBAH and DEA. Then the solution was sonicated for 30 min to completely dissolve the TM salt. The rest of the procedure was kept the same. All the samples were calcined at 500 °C for 2 h in air before the characterization and electrochemical measurements.

2.3. Material Characterization. The microstructure of the as-synthesized products was examined with a JEM−2100 (JEOL) Transmission Electron Microscope (TEM) operated at 200 kV. The crystallographic phases of the as-synthesized products were obtained by a PANalytical high resolution powder X-ray diffractometer (HR-XRD) [PW 3040/60] operated at 40 kV and 30 mA, using Cu Kα X-rays. UV−vis absorption measurements were carried out with a Cary 5000 UV−vis−NIR spectrophotometer (Agilent Tech.). The Raman measurements were carried out with a SENTERRA dispersive Raman microscope (BRUKER) at room temperature. The X-ray photoelectron spectroscopy (XPS) study was performed with use of a Thermo-VG Scientific ESCALab 250 microprobe and PHI 5000 VersaProbe II Scanning XPS Microprobe with a monochromatic Al Kα source (1486.6 eV).

2.4. Electrocatalytic Study. Electrochemical measurements were carried out with a Bipotentiostat (CH Instruments, Model: 760E) in a three-electrode system, using 1 M H_2SO_4 and in 0.1 M KOH electrolyte. The pristine and TM-doped TiO_2 NCs coated glassy carbon was used as the working electrode. Platinum wire and Ag/AgCl served as counter and reference electrodes, respectively. The potential scale was calibrated to a standard hydrogen electrode (SHE) using Potential (V) vs. SHE = Potential (V) vs. Ag/AgCl + 0.23 V for 1 M H_2SO_4 electrolyte.

3. RESULTS AND DISCUSSION

The TM doping into the TiO_2 NCs was confirmed by XRD analysis, Raman scattering, and optical measurements. Figure 1 shows the XRD patterns of pristine or undoped and TM-doped TiO_2 NCs. The diffraction features are well matched and indexed as per reference pattern (JCPDS: 00−002−0387) of pure tetragonal anatase TiO_2 suggesting that the anatase crystal structure of TiO_2 NCs does not change upon TM doping. The absence of diffraction features from TM indicates no precipitate formation of doped metal inside the NCs. In all the samples, the (101) diffraction feature is found to be the strongest indicating the major crystal growth along the same plane of anatase TiO_2.[23] Moreover, apparent shift in 2θ values (inset, Figure 1) is ascribed to TM doping. The major diffraction from the (101) Bragg plane shifted to lower 2θ, i.e. 25.55° for undoped TiO_2 NCs to 25.35° for Cu-doped TiO_2 NCs due to the lattice expansion. As the ionic size of Ti(IV) is smaller than that of corresponding TMs (II) in the same series of the periodic table,[24] TM doping increases the crystal volume resulting in the downward shift of 2θ values.

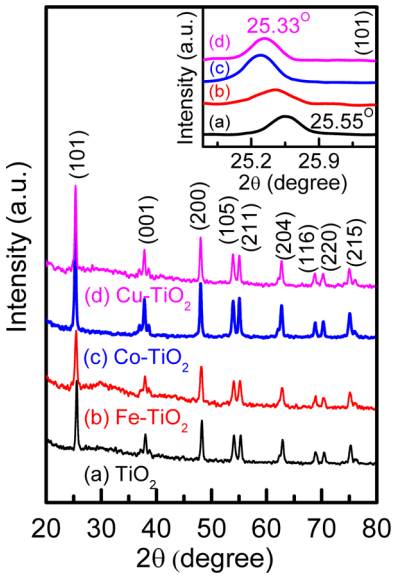

Figure 1. XRD patterns of (a) undoped, (b) Fe-doped, (c) Co-doped, and (d) Cu-doped TiO_2 NCs matching JCPDS card number 00−002−0387. The inset shows the enlarged (101) diffraction peak of undoped and TM-doped TiO_2 NCs indicating lattice expansion upon doping.

The TM doping introduces heterogeneity (due to difference in elemental property of TM and Ti in the TiO_2 crystal) in the pristine TiO_2 crystal system which has a direct effect on the bond length, bond energy, as well as bond polarizabilty. Therefore, Raman scattering is a useful technique to analyze the TM-doped TiO_2 NCs. Figure 2 shows the Raman spectra of undoped and TM-doped TiO_2 NCs. All six active Raman modes (A_{1g} + $2B_{1g}$ + $3E_g$) in anatase TiO_2 are assigned and shown in Figure 2. The prominent Raman scatterings at 141, 198, 397, 514, and 637 cm^{-1} are assigned as $E_g(1)$, $E_g(2)$, $B_{1g}(1)$, $B_{1g}(2)$ + A_{1g}, and $E_g(3)$, respectively.[25,26] The Raman peak at 141 cm^{-1} is due to the symmetric stretching of Ti−O−Ti bonds whereas peaks at 397 and 514 cm^{-1} are due to symmetric and antisymmetric bending vibrations, respectively.[27] As shown in the inset of Figure 2, an obvious shift in Raman scattering is observed for the strongest $E_g(1)$, which is shifted to a higher frequency. In particular, the $E_g(1)$ Raman mode of Cu-doped TiO_2 NCs is significantly shifted to 153 cm^{-1} from 141 cm^{-1} for undoped TiO_2 NCs (inset, Figure 2). This shift is due to the change in bond polarizability and strength of the Ti−O bond upon TM doping.

XPS analysis was carried out to further ascertain the doping of TM into TiO_2 NCs and their oxidation states.[28,29] Figure 3a shows the Ti 2p XPS region spectra of undoped and TM-doped TiO_2 NCs. The Ti $2p_{3/2}$ and $2p_{1/2}$ photoelectron peaks of undoped TiO_2 NCs are symmetric in nature and their binding energy (BE) positions are at 459.46 and 465.20 eV, respectively, revealing the Ti^{4+} state.[27] The spin−orbit splitting energy of 5.74 eV matches the literature value.[30] The Ti 2p peaks of Ti in TM-doped TiO_2 NCs are also identical with the

dx.doi.org/10.1021/jp508445t | J. Phys. Chem. C 2014, 118, 29499−29506

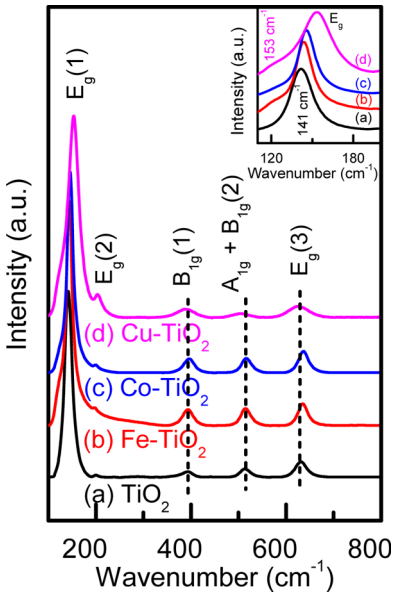

Figure 2. Raman shifts of undoped and TM-doped TiO_2 NCs depicting different vibrations of anatase TiO_2. The inset shows the shift of $E_g(1)$ peak indicating change in Ti−O bond polarizability of TM-doped TiO_2 NCs.

undoped one except for a slight positive shift in BE (0.14 eV for $2p_{3/2}$ and $2p_{1/2}$) suggesting the substitution of Ti(IV) by TMs.[28,29,31,32] This BE shift is due to the movement of electron cloud toward electronegative TMs. For example, as the Fermi levels of copper oxides are lower than that of TiO_2, electrons cloud would shift toward the Cu atom in the lattice. This would create a slight positive charge on the Ti atom leading to positive shift in BE of Ti 2p for the doped sample.[33] A similar positive shift in BE was found in the case of O 1s for TM-doped TiO_2 NCs (Figure 3b−e).[34] Figure 3b shows the O 1s XPS region spectrum of undoped TiO_2 NCs. The O 1s feature is deconvoluted to two peaks, centered at 530.62 and 531.49 eV, which can be assigned to the lattice oxygen of oxide and the adsorbed oxygen at the surface, i.e., hydroxide, respectively. Similar O 1s XPS features are observed for the TM (Fe, Co, and Cu)-doped TiO_2 NCs (Figure 3, c, d, and e, respectively). The absence of additional O 1s features in the TM-doped TiO_2 NCs suggests that TM-oxide cluster formation did not occur in the doped samples.[28] On the contrary, the BE position of O 1s is found to be shifted from 530.62 to 530.90 eV revealing the formation of skeleton −O−TM−O−TM−/−O−TM−O−Ti−. This positive shift of O 1s BE (of 0.28 eV) is due to the heteroneighbor atoms [(Fe(II), Co(II), and Cu(II)] in the skeleton. The positive shift of the O 1s BE position in the TM-doped TiO_2 NCs is found to follow the order Fe-TiO_2 < Co-TiO_2 < Cu-TiO_2 as electronegativity increases with increase in the atomic number of TM (Figure 3b−e).

The oxidation states of the doped-TMs are further obtained through the XPS analysis. Panels f, g, and h of Figure 3 show the Fe 2p, Co 2p, and Cu 2p XPS region spectra of the corresponding TM-doped TiO_2 NCs, respectively. The BE positions of Fe $2p_{3/2}$ and $2p_{1/2}$ of Fe-TiO_2 NCs are found at 709.44 and 722.89 eV, respectively, confirming the Fe(II) state.[35] The Fe region XPS spectrum shows a broad satellite peak around 716 eV, i.e. 6.5 eV above the $2p_{3/2}$ position, further suggesting the Fe(II) state in Fe-TiO_2 NCs.[36−38] The BE of Co 2p photoelectron peaks are found at 780.95 eV ($2p_{3/2}$) and 796.56 eV ($2p_{1/2}$), which suggests the Co(II) chemical state in Co-TiO_2 NCs.[24] The XPS region spectra of Co displays satellite peaks at ∼787 and ∼802 eV revealing the high spin Co(II) state with complex transitions.[24,39,40] The Cu 2p XPS spectrum (Figure 3h) shows Cu(II) $2p_{3/2}$ (932.67 eV) and $2p_{1/2}$ (952.83 eV) BE matching the reference values.[32,41] The XPS analysis revealed that all the doped TMs in the TiO_2 NCs are in the +2 oxidation state.

The morphology, size, and shape of TiO_2 NCs were further characterized by TEM and high resolution TEM (HRTEM) analysis. Figure 4 shows representative TEM and HRTEM images of TiO_2 and Cu-TiO_2 NCs. The size of the undoped

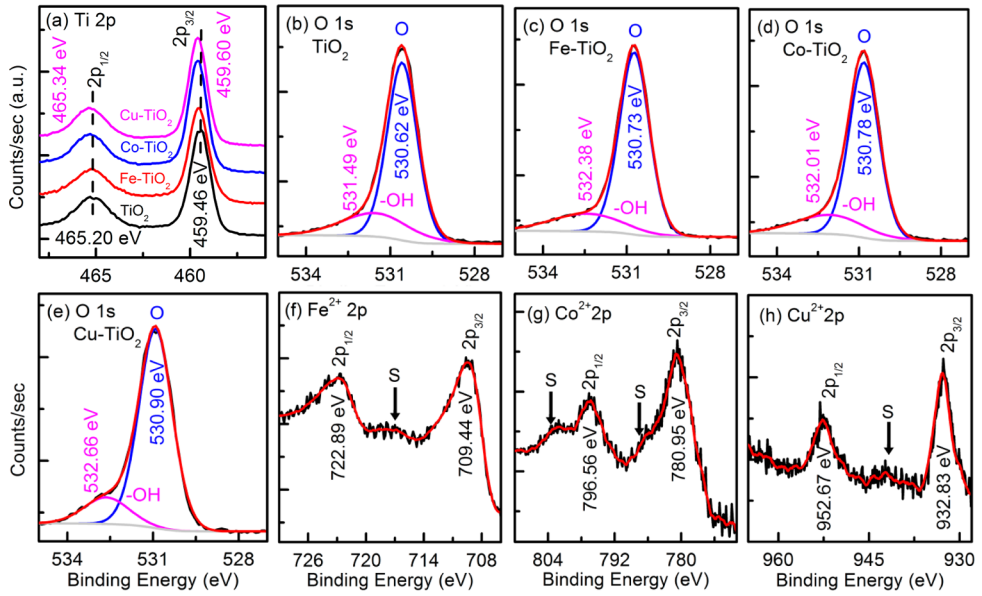

Figure 3. (a) Ti 2p XPS region spectra of undoped and TM-doped TiO_2 NCs. O 1s region spectra of (b) undoped TiO_2 NCs, (c) Fe-TiO_2 NCs, (d) Co-TiO_2 NCs, and (e) Cu-TiO_2 NCs. XPS region spectra of (f) Fe 2p of Fe-TiO_2 NCs, (g) Co 2p of Co-TiO_2 NCs, and (h) Cu 2p of Cu-TiO_2 NCs.

dx.doi.org/10.1021/jp508445t | J. Phys. Chem. C 2014, 118, 29499−29506

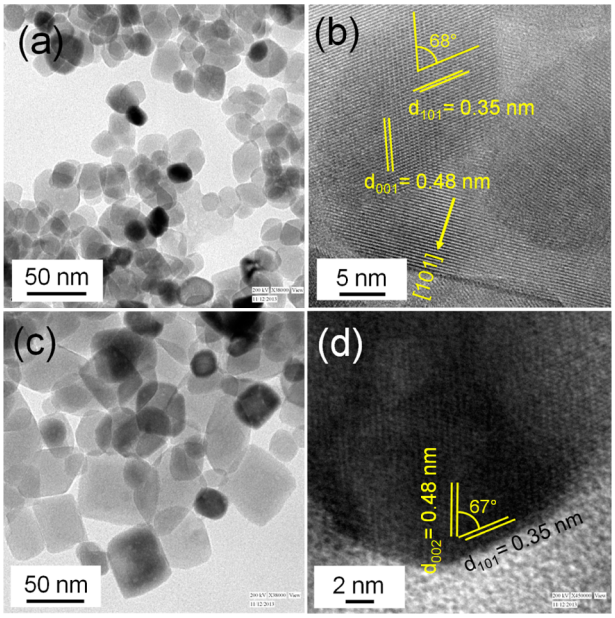

Figure 4. TEM images of (a) undoped TiO_2 and (c) Cu-TiO_2 NCs. HRTEM images of (b) undoped and (d) Cu(II)-doped TiO_2 NCs showing the continuous (002) and (101) lattice fringe of anatase TiO_2.

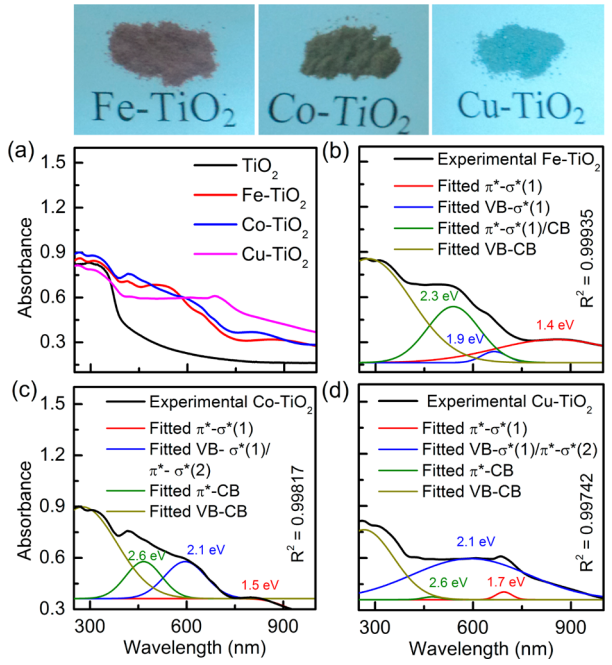

Figure 5. Across the top are digital photographs of Fe-, Co-, and Cu-doped TiO_2 NCs. (a) UV vis absorption spectra of undoped and TM-doped TiO_2 NCs displaying multiple absorption maxima in the visible region of light. Panels b–d show the deconvoluted plots of TM-doped TiO_2 NCs assigned with the energies of absorption maxima and the fit factor values.

TiO_2 NCs (Figure 4a) varies in the range of 20–40 nm. Figure 4b shows a HRTEM image clearly revealing the single crystalline nature of the NCs. The lattice fringe spacings were measured to be 0.48 and 0.35 nm corresponding to (002) and (101) planes of anatase TiO_2, respectively.[42,43] Figure 4c shows the Cu-doped TiO_2 NCs, which reveals that the morphology of NCs does not change significantly upon doping, although the average size of the Cu-TiO_2 NCs increases from 30 to 40 nm. The increase in size could be due to the incorporation of TM salts into the reaction mixture which increases the polarity of the reaction mixture and thereby increases the hydrolysis rate. The HRTEM image (Figure 4d) of Cu-TiO_2 NCs shows continuous lattice fringes further suggesting that the crystallinity remains with doping of Cu(II) in the lattice of TiO_2 NCs. Similar larger sized nanoparticles (30–50 nm) are obtained for Fe-doped (Figure S1(a,b), Supporting Information) and Co-doped (Figure S1(c,d), Supporting Information) TiO_2 NCs. The HRTEM images (Figure S1(b,d), Supporting Information) of Fe- and Co-TiO_2 NCs further suggest their highly crystalline nature.

The optical properties of TM-doped TiO_2 NCs were characterized by UV–vis absorption spectroscopy. The white color of undoped TiO_2 is found to be changed upon doping the TMs as shown in the digital photographs (top panel of Figure 5). The Fe-, Co-, and Cu-doped TiO_2 NCs powder appear reddish, olive, and sky-blue, respectively. This change in color is ascribed to doping of TM as confirmed by peak shift in the XRD, Raman scattering, and XPS analysis. Figure 5a shows the UV–vis absorption spectra of the undoped and TM-doped TiO_2 NCs revealing their light absorption properties. Absorbance sharply increases at ~400 nm for the undoped TiO_2 NCs, due to the electronic transition from valence band (VB) to conduction band (CB) matching the band gap (~3.1 eV) of TiO_2 and absorption remains low at higher wavelength (>400 nm). However, in addition to increased absorbance below 400 nm, TM-doped TiO_2 NCs absorbs substantially in the visible region with the broad absorption maxima at around 500 (Fe-TiO_2), 525 (Co-TiO_2), and 600 nm (Cu-TiO_2 NCs). The absorption in the visible region indicates multiple midgap states transitions in the TM-doped TiO_2 NCs. The transitions in the visible region can be explained on the basis of d-orbital splitting of TM in the doped TiO_2.[44] Panels b, c, and d of Figure 5 show the UV–vis absorption spectra of Fe-, Co-, and Cu-doped TiO_2 NCs and their deconvoluted absorption peaks with fit factor values. The fit factor value (R^2) of greater than 0.99 suggests the well-fitted deconvolution plots in all the cases. The energies of the absorption maxima in the deconvolution plots are assigned in the respective plots.

UV–vis absorption spectra of TM-doped TiO_2 NCs clearly reveal the multiple electronic transitions. The VB and CB of TiO_2 are composed of multiple energy levels in TiO_2 NCs.[45] The VB of TiO_2 NCs is composed of Ti–O σ, Ti–O π, and O π molecular orbitals (MOs). On the other hand, there are two theoretical CBs (lower and upper).[46] The lower CB is composed of Ti–Ti σ, Ti–Ti σ^*, Ti–Ti π, Ti–Ti π^*, and Ti–O π^* MOs while the upper CB has Ti–O σ^* MO.[45] Although the VB and CB are made up of different MOs, VB and CB have significant O 2p and Ti 3d character, respectively.[47] This is due to the higher electronegativity of O 2p than that of Ti 3d orbitals. The doped TM or nonmetal thus interacts with different MOs of TiO_2 resulting in a change in the optical properties of TiO_2. For example, in the nitrogen- or carbon-doped TiO_2, 2p states of carbon or nitrogen produce a localized state above the VB of TiO_2.[48,49] Similarly, TMs [e.g., Cu(II), Fe(II), or Mn(II)] produce the energy states above the VB and below the CB, thereby narrowing the energy gaps between the different energy levels.[47,50] The 3d-orbitals of the dicationic TMs in between the VB and CB of TiO_2 NCs can split if the geometry of the host crystal is maintained.[51] Interaction of 3d orbitals of TMs with O^{2-} of TiO_2 in an

dx.doi.org/10.1021/jp508445t | J. Phys. Chem. C 2014, 118, 29499–29506

octahedral field is known to produce three sets of MOs: (a) π^* due to interaction of the T_{2g} level of TM with the O p_π orbital, (b) $\sigma^*(1)$ due to interaction of the d_{z^2} of TM and the O p_σ orbital, and (c) $\sigma^*(2)$ due to interaction of the $d_{x^2-y^2}$ of TM with the O p_σ orbitals.[45] The energy level of π^* orbitals of TM-doped TiO_2 NCs shifts toward the VB maxima with an increase in atomic number of TM, i.e., the energy level of π^* follows the order Cu(II) < Co(II) < Fe(II).[52] On the other hand, energy levels of $\sigma^*(1)$ and $\sigma^*(2)$ are shifted upward and downward, respectively, as the atomic number of the dopant TM increases. The different electronic transitions obtained in the UV–vis spectra are therefore due to the formation of MOs which are formed upon interaction of 3d orbitals of TM with the O 2p orbitals of TiO_2 in the octahedral field. The probable energy levels of these MOs [$\sigma^*(1)$, $\sigma^*(2)$, and π^*] are displayed in Scheme 1. The absorptions at ~840 (1.4 eV), 800 (1.5 eV), and

Scheme 1. MOs in between the VB and CB of TiO_2 NCs Due to d-Orbitals Splitting of TMs and Its Bonding with O 2p Orbitals of TiO_2[a]

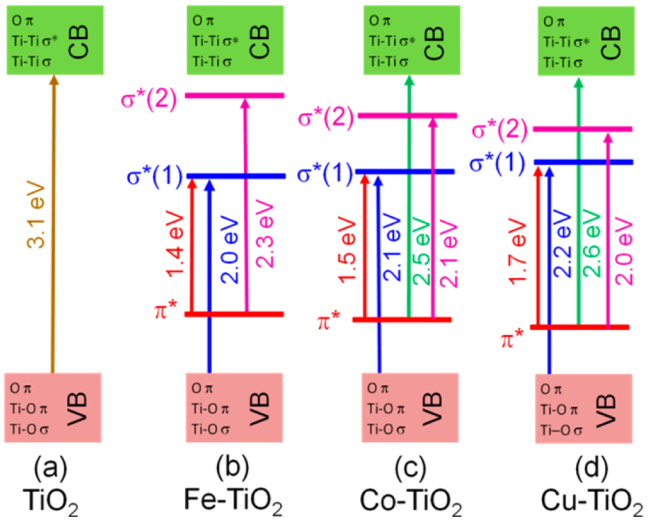

[a]The probable electronic transitions are assigned as per the absorption peaks obtained in the UV–vis absorption spectra.

700 nm (1.7 eV) are assigned to the electronic transition $\pi^* \rightarrow \sigma^*(1)$ for Fe-, Co-, and Cu-doped TiO_2 NCs, respectively, correlated with UV–vis absorption spectra (Figure 5). It should be noted that the energy of the different peak positions in the UV–vis absorption spectra is within the ±0.1 eV of transition energies marked in Scheme 1 for TM-doped TiO_2 NCs. This could be due to the slight change in VB and CB positions upon doping and/or bigger size of the dicationic TMs which introduces a slight distortion in geometry with respect to the pristine TiO_2.[52] The reddish (Fe-TiO_2), olive (Co-TiO_2), and sky-blue (Cu-TiO_2) colors can therefore be explained on the basis of deconvoluted absorption peaks (Figure 5b–d) of TM-doped TiO_2 NCs. The strongest absorption at 540 nm (2.3 eV) for Fe-TiO_2 NCs corresponds to the $\pi^* \rightarrow \sigma^*(2)$ transition (Figure 5b, Scheme 1b) correlating blue-green light and the complementary violet-reddish color is observed for the Fe-doped TiO_2 powder (Figure 5a,b, top panel). However, Co-TiO_2 shows two equally strong absorption peaks at 475 (2.6 eV) and 600 nm (2.1 eV) corresponding to $\pi^* \rightarrow$ CB and VB $\rightarrow \sigma^*(1)$ or $\pi^* \rightarrow \sigma^*(2)$ transitions, respectively (Figure 5c, Scheme 1c). These two absorption peaks correspond to blue and orange light with their complementary emission colors yellow and blue producing an olive Co-TiO_2 powder. The Cu-TiO_2 NCs show a strong and broad absorption peak at 600 nm (orange light) corresponding to VB $\rightarrow \sigma^*(1)$ or $\pi^* \rightarrow \sigma^*(2)$ transition (Figure 5d, Scheme 1d) and thereby the complementary blue Cu-TiO_2 NCs powder was obtained (Figure 5a,d, top panel]. Thus, the origin of TM-doped TiO_2 NCs powder color can be explained by the d-orbitals splitting and the formation of midgap states in between the VB and CB of TiO_2 NCs.

The TM-doping in TiO_2 NCs substantially changes its optical and electronic properties that have strong correlation to the photocatalytic properties.[53] To find the role of TM doping, we studied the electrocatalytic properties (i.e. OER) of present low temperature hydrothermally synthesized TM-doped TiO_2 NCs. Figure 6a shows the typical Mott–Schottky plots

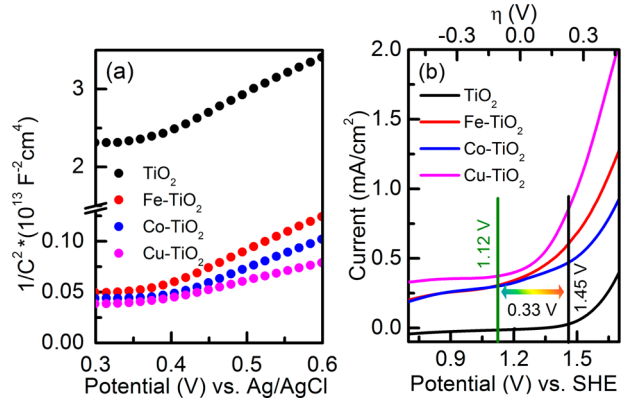

Figure 6. (a) Mott–Schottky plots of undoped and TM-doped TiO_2 NCs obtained in 1 M H_2SO_4 at 500 Hz. (b) Linear sweep voltammograms of OER with undoped and TM-doped TiO_2 NCs with respect to SHE. The upper *X*-axis shows the overpotential (η) for OER with respect to SHE at solution pH 0.

obtained with 1 M H_2SO_4 at 500 Hz. The positive slopes confirm the n-type nature of both the undoped and TM-doped TiO_2 NCs. The donor density (N_d) of undoped and TM-doped TiO_2 NCs were estimated by using the following equation, $N_d = [2/(e\varepsilon\varepsilon_0 A^2 C^2)][E - E_{FB} - (kT/e)]$, where e is the charge of an electron, C is the electrode capacitance, ε is the dielectric constant of TiO_2 (55),[54] ε_0 is the vacuum permittivity, E is the applied potential, E_{FB} is the flat band potential, k is the Boltzmann constant, T = 298 K, and A is the electrode area in cm^2 (0.07 cm^2).[54] The slope of the curve measures the extent of doping concentration. The lower the slope, the higher is the doping concentration (Figure 6a). The donor densities are estimated to be ~9.4×10^{18} (undoped TiO_2 NCs), 1.3×10^{20} (Fe-TiO_2 NCs), 1.6×10^{20} (Co-TiO_2 NCs), and 2.5×10^{20} cm^{-3} (Cu-TiO_2 NCs). Figure 6b shows linear sweep voltammetry curves for undoped and TM-doped TiO_2 NCs, depicting the OER activity. The OER begins at ~1.45 V (η = 0.22 V) for undoped TiO_2 NCs with respect to the standard hydrogen electrode (SHE), where η is the overpotential. This potential for OER is found to be drastically reduced to ~1.12 V (η = −0.11 V) for the TM-doped TiO_2 NCs due to the decrease in the overpotential of 0.33 V. Similar reduction in overpotential of 0.31 V was also observed in 0.1 M KOH electrolyte (not shown). This improved electrocatalytic property is ascribable to the change in electronic band position of TM-doped TiO_2 NCs. Recently Shi et al. reported improved

dx.doi.org/10.1021/jp508445t | J. Phys. Chem. C 2014, 118, 29499–29506

electrochemical activity of TiO_2 upon tuning its electronic properties.[55] The lower overpotential for OER with TM-doped TiO_2 NCs is believed to be due to higher adsorption and decomposition of reaction intermediates ($OOH^•$, $OH^•$, and $O^•$) at the catalyst surface.[15,55] Scheme 2 shows the representative well-known oxidation potentials for different moieties in OER for Cu-TiO_2 NCs and its electronic energy band positions of midgap states, i.e. $\sigma^*(1)$ and $\sigma^*(2)$ (based in Scheme 1), which are formed due to TM (Cu) doping with respect to SHE.[56−58] The $\sigma^*(1)$ and $\sigma^*(2)$ MOs are axis directed in an octahedral field and their energy levels lie near the peroxide and water oxidation potentials. Therefore, they are likely to interact with the σ orbitals of the intermediate species ($OOH^•$, $OH^•$, and $O^•$) thereby reducing the overpotential of OER. The decrease in OER overpotential with the TM-doped catalyst is therefore attributed to the formation of midgap states in between the CB and VB of TiO_2 NCs due to d-orbital splitting of TMs. Furthermore, current densities obtained with TM-doped TiO_2 NCs are higher than that of undoped TiO_2 NCs. The higher current densities with TM-doped TiO_2 NCs can be attributed to higher electronic conductivity with increase in their carrier concentrations upon doping as confirmed from the Mott−Schottky plots.

Scheme 2. Electronic Band Positions of Cu-Doped TiO_2 NCs and Oxidation Potentials for Peroxide and Water in OER

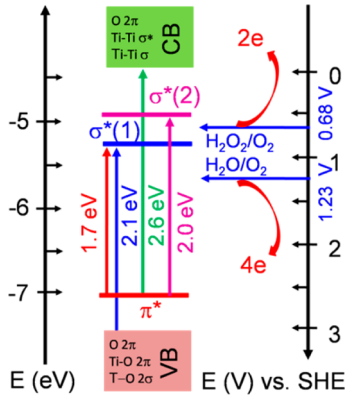

4. CONCLUSIONS

In conclusion, we demonstrate here the improved optical and electrocatalytic properties of hydrothermally synthesized TM-doped TiO_2 NCs. The deviation of pearl white pristine TiO_2 NCs color for the TM-doped TiO_2 NCs is ascribed to the d-orbital splitting of TM and its interaction with the O p orbitals forming MOs [π^*, $\sigma^*(1)$, $\sigma^*(2)$], in between the VB and CB of TiO_2. Such splitting and formation of midgap states significantly increases the light absorption properties in the visible range and improved the electrocatalytic properties due to the interaction of split energy levels with intermediate peroxide species of water oxidation. In particular, TM-doped TiO_2 NCs exhibit marked reduction in the overpotential of OER as compared to the undoped TiO_2 NCs. Thus, the present study demonstrates that the tuning of energy levels in between the VB and CB is one of the key parameters to the performance of TiO_2 NCs as an anode electrocatalyst in PEM water electrolyzers.

■ ASSOCIATED CONTENT

Ⓢ Supporting Information

TEM and HRTEM images of Fe-doped and Co-doped TiO_2 NCs. This material is available free of charge via the Internet at http://pubs.acs.org.

■ AUTHOR INFORMATION

Corresponding Author

* E-mail: deb@matsc.iitkgp.ernet.in. Tel: +91-3222-281798.

Notes

The authors declare no competing financial interest.

■ ACKNOWLEDGMENTS

This work was funded by the Council of Scientific and Industrial Research [Grant No. 01(2724)/13/EMR-II] and National Research Foundation of Korea, MEST (NRF-2012R1A1A4A01005645). One of the authors (N.R.) acknowledges CSIR, New Delhi for a fellowship. K.T.L. is grateful for the support of the Natural Sciences and Engineering Research Council of Canada.

■ REFERENCES

(1) Walter, M. G.; Warren, E. L.; McKone, J. R.; Boettcher, S. W.; Mi, Q.; Santori, E. A.; Lewis, N. S. Solar Water Splitting Cells. *Chem. Rev.* **2010**, *110*, 6446−6473.

(2) Rossmeisl, J.; Qu, Z.-W.; Zhu, H.; Kroes, G.-J.; Nørskov, J. K. Electrolysis of Water on Oxide Surfaces. *J. Electroanal. Chem.* **2007**, *607*, 83−89.

(3) Hu, C.; Zhang, X.; Li, W.; Yan, Y.; Xi, G.; Yang, H.; Li, J.; Bai, H. Large-scale, Ultrathin and (001) Facet Exposed TiO_2 Nanosheet Superstructures and their Applications in Photocatalysis. *J. Mater. Chem. A* **2014**, *2*, 2040−2043.

(4) Morterra, C.; Cerrato, G.; Viscab, M.; Lenti, D. M. Surface Characterization of Some TiO_2-Based Pigments. Part 3. Coating of the Pigments. *J. Mater. Chem.* **1992**, *2*, 341−355.

(5) Yun, H.-G.; Park, J. H.; Bae, B. A.; Kang, M. G. Dye-sensitized Solar Cells with TiO_2 Nano-particles on TiO_2 Nano-tube-grown Ti Substrates. *J. Mater. Chem.* **2011**, *21*, 3558−3561.

(6) Zaleska, A. Doped-TiO_2: A Review. *Recent Pat. Eng.* **2008**, *2*, 157−164.

(7) Su, R.; Bechstein, R.; Kibsgaard, J.; Vang, R. T.; Besenbacher, F. High-quality Fe-doped TiO_2 Films with Superior Visible-light Performance. *J. Mater. Chem.* **2012**, *22*, 23755−23758.

(8) Yang, G.; Jiang, Z.; Shi, H.; Xiao, T.; Yan, Z. Preparation of Highly Visible-light Active N-doped TiO_2 Photocatalyst. *J. Mater. Chem.* **2010**, *20*, 5301−5309.

(9) Arashi, T.; Seo, J.; Takanabe, K.; Kubota, J.; Domen, K. Nb-doped TiO_2 Cathode Catalysts for Oxygen Reduction Reaction of Polymer Electrolyte Fuel Cells. *Catal. Today* **2014**, *233*, 181−186.

(10) Chevallier, L.; Bauer, A.; Cavaliere, S.; Hui, R.; Rozière, J.; Jones, D. J. Mesoporous Nanostructured Nb-Doped Titanium Dioxide Microsphere Catalyst Supports for PEM Fuel Cell Electrodes. *ACS Appl. Mater. Interfaces* **2012**, *4*, 1752−1759.

(11) Hu, W.; Chen, S.; Xia, Q. IrO_2/Nb−TiO_2 Electrocatalyst for Oxygen Evolution Reaction in Acidic Medium. *Int. J. Hydrogen Energy* **2014**, *39*, 6967−6976.

(12) Audichona, T.; Mayousse, E.; Napporn, T. W.; Moraisa, C.; Comminges, C.; Kokoha, K. B. Elaboration and Characterization of Ruthenium Nano-oxides for the Oxygen Evolution Reaction in a Proton Exchange Membrane Water Electrolyzer Supplied by a Solar Profile. *Electrochim. Acta* **2014**, *132*, 284−291.

(13) Lim, J. Y.; Rahman, G.; Chae, S. Y.; Lee, K.-Y.; Kim, C.-S; Joo, O.-S. Highly Stable RuO_2/SnO_2 Nanocomposites as Anode Electrocatalysts in a PEM Water Electrolysis Cell. *Int. J. Energy Res.* **2014**, *38*, 875−883.

(14) Stoerzinger, K. A.; Qiao, L.; Biegalski, M. D.; Shao-Horn, Y. Orientation-Dependent Oxygen Evolution Activities of Rutile IrO_2 and RuO_2. *J. Phys. Chem. Lett.* **2014**, *5*, 1636−1641.
(15) Chen, J.; Li, Y.-F.; Sit, P.; Selloni, A. Chemical Dynamics of the First Proton-Coupled Electron Transfer of Water Oxidation on TiO_2 Anatase. *J. Am. Chem. Soc.* **2013**, *135*, 18774−18777.
(16) Jung, J.-I.; Jeong, H. Y.; Lee, J.-S.; Kim, M. G.; Cho, J. A Bifunctional Perovskite Catalyst for Oxygen Reduction and Evolution. *Angew. Chem., Int. Ed.* **2014**, *53*, 4582−4586.
(17) Zhuang, Z.; Sheng, W.; Yan, Y. Synthesis of Monodispere Au@Co_3O_4 Core-Shell Nanocrystals and Their Enhanced Catalytic Activity for Oxygen Evolution Reaction. *Adv. Mater.* **2014**, *26*, 3950−3955.
(18) Gao, M.; Sheng, W.; Zhuang, Z.; Fang, Q.; Gu, S.; Jiang, J.; Yan, Y. Efficient Water Oxidation Using Nanostructured α-Nickel-Hydroxide as an Electrocatalyst. *J. Am. Chem. Soc.* **2014**, *136*, 7077−7084.
(19) Trotochaud, L.; Young, S. L.; Ranney, J. K.; Boettcher, S. W. Nickel−Iron Oxyhydroxide Oxygen-Evolution Electrocatalysts: The Role of Intentional and Incidental Iron Incorporation. *J. Am. Chem. Soc.* **2014**, *136*, 6744−6753.
(20) Cai, L.; Cho, I. S.; Logar, M.; Mehta, A.; He, J.; Lee, C. H.; Rao, P. M.; Feng, Y.; Wilcox, J.; Prinz, F. B.; et al. Sol-flame Synthesis of Cobalt-doped TiO_2 Nanowires with Enhanced Electrocatalytic Activity for Oxygen Evolution Reaction. *Phys. Chem. Chem. Phys.* **2014**, *16*, 12299−12306.
(21) Liu, B.; Chen, H. M.; Liu, C.; Andrews, S. C.; Hahn, C.; Yang, P. Large-Scale Synthesis of Transition-Metal-Doped TiO_2 Nanowires with Controllable Overpotential. *J. Am. Chem. Soc.* **2013**, *135*, 9995−9998.
(22) Resasco, J.; Dasgupta, N. P.; Rosell, J. R.; Guo, J.; Yang, P. Uniform Doping of Metal Oxide Nanowires Using Solid State Diffusion. *J. Am. Chem. Soc.* **2014**, *136*, 10521−10526.
(23) Roy, N.; Sohn, Y.; Pradhan, D. Synergy of Low-Energy {101} and High-Energy {001} TiO_2 Crystal Facets for Enhanced Photocatalysis. *ACS Nano* **2013**, *7*, 2532−2540.
(24) Zhang, H.; Ji, T.; Liu, Y.; Cai, J. Preparation and Characterization of Room Temperature Ferromagnetic Co-Doped Anatase TiO_2 Nanobelts. *J. Phys. Chem. C* **2008**, *112*, 8604−8608.
(25) Balachandran, U.; Eror, N. G. Raman Spectra of Titanium Dioxide. *J. Solid State Chem.* **1982**, *42*, 276−282.
(26) Frank, O.; Zukalova, M.; Laskova, B.; Kurti, J.; Koltai, J.; Kavan, L. Raman Spectra of Titanium Dioxide (anatase, rutile) with Identified Oxygen Isotopes (16, 17, 18). *Phys. Chem. Chem. Phys.* **2012**, *14*, 14567−14572.
(27) Tian, F.; Zhang, Y.; Zhang, J.; Pan, C. Raman Spectroscopy: A New Approach to Measure the Percentage of Anatase TiO_2 Exposed (001) Facets. *J. Phys. Chem. C* **2012**, *116*, 7515−7519.
(28) Li, J.; Zeng, H. C. Hollowing Sn-Doped TiO_2 Nanospheres via Ostwald Ripening. *J. Am. Chem. Soc.* **2007**, *129*, 15839−15847.
(29) Liu, M.; Qiu, X.; Miyauchi, M.; Hashimoto, K. Energy-Level Matching of Fe(III) Ions Grafted at Surface and Doped in Bulk for Efficient Visible-Light Photocatalysts. *J. Am. Chem. Soc.* **2013**, *135*, 10064−10072.
(30) Papageorgiou, A. C.; Cabailh, G.; Chen, Q.; Resta, A.; Lundgren, E.; Andersen, J. N.; Thornton, G. Growth and Reactivity of Titanium Oxide Ultrathin Films on Ni(110). *J. Phys. Chem. C* **2007**, *111*, 7704−7710.
(31) Duan, Y.; Fu, N.; Liu, Q.; Fang, Y.; Zhou, X.; Zhang, J.; Lin, Y. Sn-Doped TiO_2 Photoanode for Dye-Sensitized Solar Cells. *J. Phys. Chem. C* **2012**, *116*, 8888−8893.
(32) Pan, L.; Zou, J.-J.; Zhang, X.; Wang, L. Photoisomerization of Norbornadiene to Quadricyclane Using Transition Metal Doped TiO_2. *Ind. Eng. Chem. Res.* **2010**, *49*, 8526−8531.
(33) Xin, B.; Wang, P.; Ding, D.; Liu, J.; Ren, Z.; Fu, H. Effect of Surface Species on Cu-TiO_2 Photocatalytic Activity. *Appl. Surf. Sci.* **2008**, *254*, 2569−2574.
(34) Rocha, V. M. S.; Pereira, M. G.; Teles, L. R.; Souza, M. O. G. Effect of Copper on the Photocatalytic Activity of Semiconductor-based Titanium Dioxide (anatase) and Hematite (α-Fe_2O_3). *Mater. Sci. Eng., B* **2014**, *185*, 13−20.
(35) Wang, S.; Lian, J. S.; Zheng, W. T.; Jiang, Q. Photocatalytic Property of Fe Doped Anatase and Rutile TiO_2 Nanocrystal Particles Prepared by Sol−Gel Technique. *Appl. Surf. Sci.* **2012**, *263*, 260−265.
(36) Brundle, C. R.; Chguang, T. J.; Wandelt, K. Core and Valence Level Photoemission Studies of Iron Oxide Surface and the Oxidation of Iron. *Surf. Sci.* **1977**, *68*, 459−468.
(37) Garat, P. C. J.; Somers, M. A. J. Simultaneous Determination of Composition and Thickness of Thin Iron-Oxide Films from XPS Fe 2p Spectra. *Appl. Surf. Sci.* **1996**, *100*, 36−40.
(38) Grosvenor, A. P.; Kobe, B. A.; Biesinger, M. C.; McIntyre, N. S. Investigation of Multiplet Splitting of Fe 2p XPS Spectra and Bonding in Iron Compounds. *Surf. Interface Anal.* **2004**, *36*, 1564−1574.
(39) Petitto, S. C.; Marsh, E. M.; Carson, G. A.; Langell, M. A. Cobalt Oxide Surface Chemistry: The Interaction of CoO(100), Co_3O_4(110), and Co_3O_4(111) with Oxygen and Water. *J. Mol. Catal. A: Chem.* **2008**, *281*, 49−58.
(40) Fu, B. L.; Liu, Z.; Liu, Y.; Han, B.; Hu, P.; Cao, L.; Zhu, D. Beaded Cobalt Oxide Nanoparticles along Carbon Nanotubes: Towards More Highly Integrated Electronic Devices. *Adv. Mater.* **2005**, *17*, 217−221.
(41) Colon, G.; Maicu, M.; Hidalgo, M. C.; Navıo, J. A. Cu-doped TiO_2 Systems with Improved Photocatalytic Activity. *Appl. Catal., B* **2006**, *67*, 41−51.
(42) Nguyen, C. K.; Cha, H. G.; Kang, Y. S. Axis-Oriented, Anatase TiO_2 Single Crystals with Dominant {001} and {100} Facets. *Cryst. Growth Des.* **2011**, *11*, 3947−3953.
(43) Zhu, J.; Wang, S.; Bian, Z.; Xie, S.; Cai, C.; Wang, J.; Yangb, H.; Li, H. Solvothermally Controllable Synthesis of Anatase TiO_2 Nanocrystals with Dominant {001} Facets and Enhanced Photocatalytic Activity. *CrystEngComm* **2010**, *12*, 2219−2224.
(44) Harb, M. Screened Coulomb Hybrid DFT Study on Electronic Structure and Optical Properties of Anionic and Cationic Te-Doped Anatase TiO_2. *J. Phys. Chem. C* **2013**, *117*, 12942−12948.
(45) Umebayashi, T.; Yamaki, T.; Itoh, H.; Asai, K. Analysis of Electronic Structures of 3d Transition Metal-doped TiO_2 Based on Band Calculations. *J. Phys. Chem. Solid* **2002**, *63*, 1909−1920.
(46) Sorantin, P. I.; Schwarz, K. Chemical Bonding in Rutile-Type Compounds. *Inorg. Chem.* **1992**, *31*, 567−576.
(47) Pereira, A. J.; Gracia, L.; Beltrán, A.; Lisboa-Filho, P. N.; da Silva, J. S. D.; Andrés, J. Structural and Electronic Effects of Incorporating Mn in TiO_2 Films Grown by Sputtering: Anatase versus Rutile. *J. Phys. Chem. C* **2012**, *116*, 8753−8762.
(48) Wang, J.; Tafen, D. N.; Lewis, J. P.; Hong, Z.; Manivannan, A.; Zhi, M.; Li, M.; Wu, N. Origin of Photocatalytic Activity of Nitrogen-Doped TiO_2 Nanobelts. *J. Am. Chem. Soc.* **2009**, *131*, 12290−12297.
(49) Chen, X.; Burda, C. The Electronic Origin of the Visible-Light Absorption Properties of C-, N- and S-Doped TiO_2 Nanomaterials. *J. Am. Chem. Soc.* **2008**, *130*, 5018−5019.
(50) Thimsen, E.; Biswas, S.; Lo, C. S.; Biswas, P. Predicting the Band Structure of Mixed Transition Metal Oxides: Theory and Experiment. *J. Phys. Chem. C* **2009**, *113*, 2014−2021.
(51) Huhee, J. E.; Keiter, E. A.; Keiter, R. L. *Inorganic Chemistry: Principles of Structure and Reactivity*, 4th ed.; HarperCollins College Publishers: New York, NY; 387−471.
(52) Wang, Y.; Zhang, R.; Li, J.; Li, L.; Lin, S. First-principles Study on Transition Metal-doped Anatase TiO_2. *Nano Res. Lett.* **2014**, *9*, 46−53.
(53) Hachiya, A.; Takata, S.; Komuro, Y.; Matsumoto, Y. Effects of V-Ion Doping on the Photoelectrochemical Properties of Epitaxial TiO_2(110) Thin Films on Nb-Doped TiO_2 (110) Single Crystals. *J. Phys. Chem. C* **2012**, *116*, 16951−16956.
(54) Kavan, L.; Tétreault, N.; Moehl, T.; Grätzel, M. Electrochemical Characterization of TiO_2 Blocking Layers for Dye-Sensitized Solar Cells. *J. Phys. Chem. C* **2014**, *118*, 16408−16418.
(55) Shi, F.; Baker, L. R.; Hervier, A.; Somorjai, J. A.; Komvopoulos, K. Tuning the Electronic Structure of Titanium Oxide Support to

Enhance the Electrochemical Activity of Platinum Nanoparticles. *Nano Lett.* **2013**, *13*, 4469−4474.
(56) Wang, W.-N.; An, W.-J.; Ramalingam, B.; Mukherjee, S.; Niedzwiedzki, D. M.; Gangopadhyay, S.; Biswas, P. Size and Structure Matter: Enhanced CO_2 Photoreduction Efficiency by Size-Resolved Ultrafine Pt Nanoparticles on TiO_2 Single Crystals. *J. Am. Chem. Soc.* **2012**, *134*, 11276−11281.
(57) Liu, M.; Qiu, X.; Miyauchi, M.; Hashimoto, K. Cu(II) Oxide Amorphous Nanoclusters Grafted Ti^{3+} Self-Doped TiO_2: An Efficient Visible Light Photocatalyst. *Chem. Mater.* **2011**, *23*, 5282−5286.
(58) Yu, H.; Irie, H.; Shimodaira, Y.; Hosogi, Y.; Kuroda, Y.; Miyauchi, M.; Hashimoto, K. An Efficient Visible-Light-Sensitive Fe(III)-Grafted TiO_2 Photocatalyst. *J. Phys. Chem. C* **2010**, *114*, 16481−16487.